Available online at www.sciencedirect.com

jmr&t Journal of Materials Research and Technology

journal homepage: www.elsevier.com/locate/jmrt

Original Article

Welding behavior of an ultrahigh-strength quenching and partitioning steel by fusion and solid-state welding methods

Z.W. Wang [a,c,d], M. Liu [c,d], H. Zhang [a,c], G.M. Xie [b], P. Xue [a,c,*], L.H. Wu [a,c], Z. Zhang [a,c], D.R. Ni [a,c], B.L. Xiao [a,c], Z.Y. Ma [a,c]

[a] CAS Key Laboratory of Nuclear Materials and Safety Assessment, Institute of Metal Research, Chinese Academy of Sciences, Shenyang 110016, China

[b] State Key Laboratory of Rolling and Automation, Northeastern University, Shenyang 110819, China

[c] Shi-changxu Innovation Center for Advanced Materials, Institute of Metal Research, Chinese Academy of Sciences, Shenyang 110016, China

[d] School of Materials Science and Engineering, University of Science and Technology of China, Shenyang 110016, China

ARTICLE INFO

Article history:
Received 3 December 2021
Accepted 18 January 2022
Available online 22 January 2022

Keywords:
Ultrahigh-strength steel
Fusion welding
Friction stir welding
Microstructure
Mechanical property
Welding behavior

ABSTRACT

How the quenching and partitioning (Q&P) steel with an ultrahigh strength (>1 GPa) behaves during the welding process is a considerable issue for its practical application, but the systematical evaluation on the welding behavior of this new steel has not yet been concerned. Here the structure-property relationships of three typical Q&P 1180 steel joints were comparatively studied by using laser welding (LW), tungsten inert gas (TIG) welding, and friction stir welding (FSW). Weld metal (WM) region and heat-affected zone were generated in the welded joints and their widths were mainly related to the welding linear energy (LW < FSW < TIG welding). During LW and TIG welding, the parent metal (PM) was totally destroyed and coarsened in the WMs whereas ultrafine microstructures with high hardness were obtained after FSW by means of the low peak temperature and severe plastic deformation. The TIG welding produced serious material softening, while the softening degree could be alleviated via LW and FSW. Excellent tensile strength as high as that of the PM was achieved in both the LW and FSW joints by means of the suppressed material softening as well as small soft zone width. However, dramatic losses of strength and ductility were found in the TIG welded joint owing to the premature strain localization and fracture in the soft zone.

* Corresponding author.
E-mail address: pxue@imr.ac.cn (P. Xue).

https://doi.org/10.1016/j.jmrt.2022.01.086

1. Introduction

Quenching and partitioning (Q&P) steels are now widely developed as alternative steels for weight reduction of the automotive body in white to promote energy conservation and emission reduction. This kind of steels commonly offers desirable strength-ductility synergies arising from their multiphase, metastable, and multiscale structures, which are obtained through a quenching-partitioning process followed by secondary quenching [1]. The quenching treatment can produce hard martensite to enhance the strength, while the partitioning route enables the stable preservation of austenite under ambient temperature to afford plasticity by transformation-induced plasticity (TRIP) effect [2,3]. These unique microstructures of Q&P steels result in a higher tensile strength together with a larger elongation than conventional high strength low alloy (HSLA) steel as well as advanced high-strength steels (AHSSs) of martensitic steel, TRIP steel and dual-phase (DP) steel [4,5].

Welding, an imperative procedure during assembling the structural components, has played a crucial role in the manufacture of automobiles since high-quality welded joints are required to ensure the vehicle body's safety. However, the thermal effect during welding often worsens the mechanical performance of AHSSs. Previous researches have shown that apparent material softening could be detected during various welding methods, such as laser welding (LW) [6–8], resistance spot welding (RSW) [9–11], gas metal arc welding (GMAW) [6,12] or friction stir welding (FSW) [13–16], for AHSSs like DP steel [6,9,12–14], TRIP steel [7,15,17], and martensitic steel [8,12,17]. Most of the property losses are related to the grain coarsening or tempering decomposition of parent metal (PM) due to high-temperature duration, and thus produces heterogeneous microstructures in a softened heat-affected zone (HAZ) where local stress or strain concentration is preferentially developed during deformation.

The microstructural characteristic of the PM and welding method adopted are two critical factors in suppressing the property deterioration of HAZ and achieving high-quality tailored-welded blanks [18]. The Q&P treatment is a promising method to fabricate Q&P steels with more stable inner structures, since the recovery of martensite can proceed during carbon partitioning into austenite with consequent austenite stabilization [2,19–21]. Recent studies have verified the excellent jointing performance of Q&P 980 steels during LW [22–24] and FSW [25,26], and equal strength joints to PM were successfully fabricated with negligible HAZ softening. Wang et al. [27] have demonstrated the feasibility of achieving high strength joints in an ultrahigh strength Q&P 1180 steel, while comparable strength joint is hard to realize in DP steel [16] and TRIP steel [15] of similar strength level.

The welding method can also determine the joint's performance because the dimension as well as softening degree of the HAZ can be significantly different under diverse heat source energies, welding speeds and cooling rates [6,28,29]. Although several works have shown attractive welding performance of Q&P steels [22,23,25,27,30], the comprehensive consideration of the welding method and the resultant influence on the microstructure and mechanical properties of Q&P steels, especially those possessed ultrahigh strength (>1 GPa), is still poorly understood thus far. The crosswise comparison of different welding methods can not only comprehend the weldability of Q&P steel in depth, but also help to provide an optimum welding method for high-quality Q&P steel joints.

This work directs at understanding the structure-property evolution of the ultrastrong Q&P 1180 steel joints under diversified welding methods. Three typical welding processes, fusion welding approaches of traditional tungsten inert gas (TIG) welding, high-energy beam LW and typical solid-state welding technique of FSW, were adopted to fabricate defect-free joints. The macrostructures and microstructures across the joints were comparatively studied to appreciate the mechanical behavior evolution and failure locations of the welded joints, and the correlations among welding methods, microstructures and mechanical properties of Q&P steel joints were discussed.

2. Materials and methods

2.1. Parent material

Cold-rolled 1.6 mm thick Q&P 1180 steel sheets with a chemical composition presented in Table 1 were used as the PM. This steel owns a yield strength (YS) of 1048 MPa, an ultimate tensile strength (UTS) of 1214 MPa, and a total elongation (TEL) of 15%. The microstructure and phase component of the PM were exhibited in Fig. 1. Complex phases including martensite (M), ferrite (F) and retained austenite (RA) were observed. The percentage of ferrite and retained austenite was 11.7% and 7.8% respectively (volume fraction). The rest was martensite which could be subdivided into initial martensite (M_I, produced in the initial quenching stage) and fresh martensite (M_F, developed in the secondary quenching stage) [30]. The grain structure of the PM was in an ultrafine scale with an average size of 0.6 μm.

2.2. Welding methods

Three typical welding methods of LW, TIG welding, and FSW were applied to the PM to fabricate weld seams along the rolling direction (RD). Therein, LW and TIG welding are frequently-used fusion methods for welding steels [31], while FSW is a solid-state welding technology that has the capability of achieving high-quality steel joints [32–34]. A 1.6 kW fiber laser was used during LW with a welding speed of 1.5 m/min. A voltage-current collocation of 14 V–80 A was adopted in the TIG welding process with a welding speed of 0.2 m/min. The refractory alloy (W-25Re) was selected to fabricate the rotational tool used in FSW, during which a consistent tool rotation rate and a moving speed of 300 rpm and 0.2 m/min were exerted respectively. In order to eliminate the probable defect

Table 1 – Chemical constituent of the Q&P 1180 steel (wt %).

C	Mn	Si	Al	S	P	Fe
0.19	2.76	1.60	0.039	0.003	0.01	Bal.

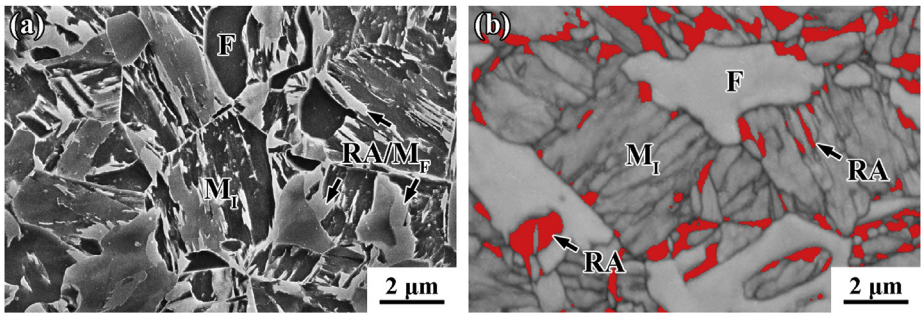

Fig. 1 – Microstructural morphology of the Q&P 1180 steel observed by (a) SEM, (b) EBSD.

Table 2 – Welding parameters and geometries of the three joints.

Welding method	Power P (kW)	Welding speed v (m/min)	Linear energy E_l (kJ/m)	Max width of WM (mm)
LW	1.60	1.5	64	1.24
TIG	1.12	0.2	336	3.82
FSW	0.46	0.2	138	10.91

induced by the butting interface, a bead-on-plate configuration was conducted without filler wire for all of the three welding procedures.

Linear energy E_l (J/m), the average energy deposited per unit path length, is a key parameter to evaluate the heat input of welding methods on the as-welded PM. The E_l can be given as [35]:

$$E_l = \frac{P}{v} \tag{1}$$

where P and v are the heat source power output (W) and moving speed (m/s). Note the E_l would be evaluated without considering the energy absorption efficiency for simplification (the same below). In this work, the welding speeds and power output of LW (P_{LW}) are currently available parameters, while P_{TIG} and P_{FSW} can be calculated as follows [36,37]:

$$P_{TIG} = UI \tag{2}$$

$$P_{FSW} = \frac{4}{3}\pi^2 \mu \sigma R^3 \tag{3}$$

where U and I are the welding voltage (V) and current (A), μ the friction coefficient between rotational tool and PM (0.41-0.28 for steel [38]), ω and R the rotational rate (rot/s) and geometric radius (m) of the tool, σ is the contact pressure (Pa) of the workpiece exerted by the welder spindle and can be given by

$$\sigma = \frac{F}{\pi R^2} \tag{4}$$

where F is the axial load (N). Hence, Eq. (3) can be simplified as

$$P_{FSW} = \frac{4}{3}\pi \mu F \omega R \tag{5}$$

In the present study, μ is taken as 0.4 [39], F is 10 kN after measurement, ω is 5 rot/s, and R is 5.5 mm. Based on the above equations and parameters, the E_l of each welding method can be obtained as shown in Table 2.

2.3. Microstructural characterization

The cross-sections of the different joints were observed by optical microscope (OM, Leica DMi8M) and scanning electron microscope (SEM, FEI Inspect F50). Electron backscatter

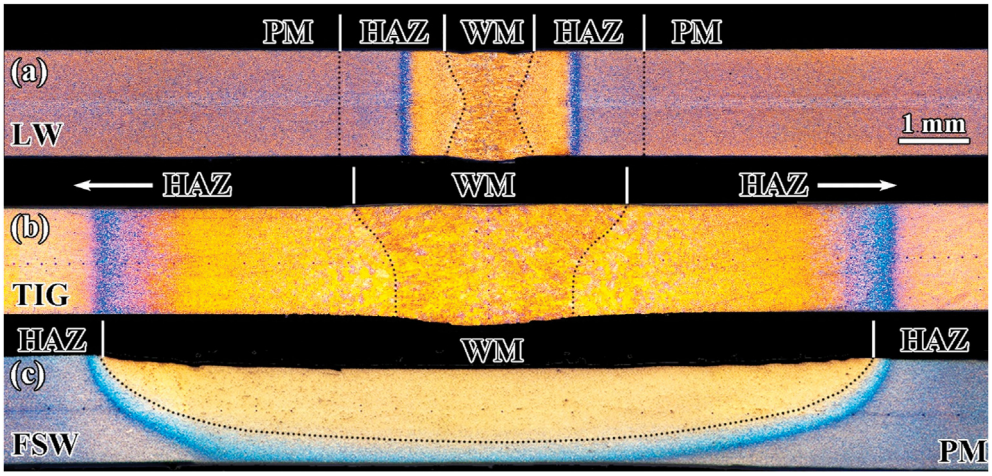

Fig. 2 – Cross-sectional macromorphologies of the Q&P 1180 steel joints after (a) LW, (b) TIG welding and (c) FSW.

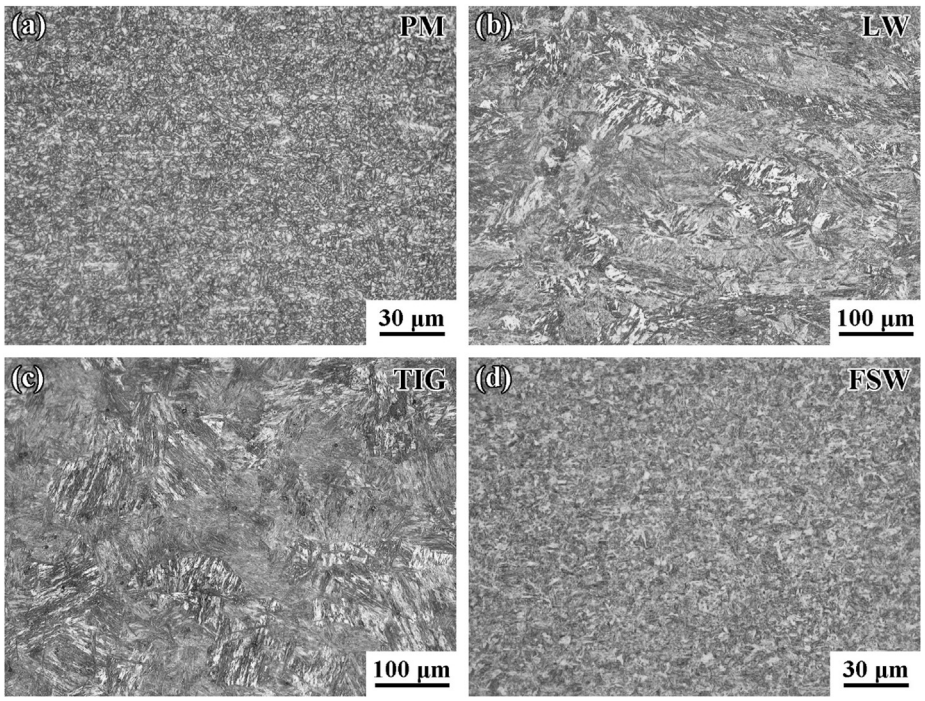

Fig. 3 – Optical images of the PM (a) and the WMs under LW (b), TIG welding (c) and FSW (d).

diffraction (EBSD, Channel 5 software, step size 0.04 μm) technique was adopted to examine the grain size and phase component. Note that the automatic image analysis method was adopted to measure the ferrite volume fraction according to ASTM E1245 standard [40] via SEM images owing to the comparable crystalline structure of ferrite and martensite. The OM and SEM samples were etched with 5% Nital after being ground and polished, while electrochemical polishing was applied to the EBSD specimens in 10% perchloric acid alcohol solution at 20 V, −25 °C.

2.4. *Mechanical assessment*

Vickers hardness was measured on the OM specimens adopting a 200 g applied load with a 15s dwell time along the thickness center. Dog-bone-shaped tensile specimens were cut perpendicular to the RD with a gauge dimension of $40 \times 6 \times 1.6\ mm^3$ according to ASTM E8 standard [41], and then were tested using an Instron 8801 machine at room temperature under a consistent crosshead moving speed of 2.4 mm/min. The local strain evolution of the joints was evaluated by the digital image correlation (DIC) procedure. With the tensile test proceeding, two high-speed industrial cameras captured the in-situ images on the speckled cross-sections with a collection frequency of 5 frames/s.

3. Results and discussion

3.1. *Macromorphology*

Fig. 2 displays the cross-sectional macromorphologies of the three welded joints. Defect-free joints were successfully produced. Three differentiated zones which consisted of weld metal (WM), HAZ and PM were observed across the joints even if obvious differences existed in the morphology and dimension among the three joints. Saddle-shaped, funnel-shaped and basin-shaped WMs were formed in the LW, TIG welding and FSW joint, respectively. The maximum width of the WM was measured as shown in Table 2, it was apparent that the LW possessed the smallest WM due to the lowest linear energy, while the FSW produced the largest WM because of a large heat source area which was controlled by the tool shoulder diameter.

3.2. *Microstructure*

The microstructural characteristic of a welded joint was highly dependent on the thermal cycle and strain condition during welding. For LW and TIG welding, the peak temperatures could surpass ~1500 °C due to materials remelting. After that, high-temperature duration and air cooling proceeded with phase transformation of liquid → austenite → martensite, during which a rapid grain growth of austenite occurred at elevated temperature. Therefore, the PM was demolished in the WMs (Fig. 3a–c) and coarse martensite with an apparent lath substructure was observed in the LW and TIG welding joints (Fig. 4a and d). According to our previous study [27], the peak temperature during the present FSW process should be near the A_{c3} temperature of 847 °C, which was greatly lower than that of the LW and TIG welding. During high-temperature duration and austenitization, severe plastic deformation and dynamic recrystallization occurred via tool stirring, resulting in significant grain refinement of austenite. Then, refined martensite was generated via the solid-state phase transformation of austenite → martensite under air

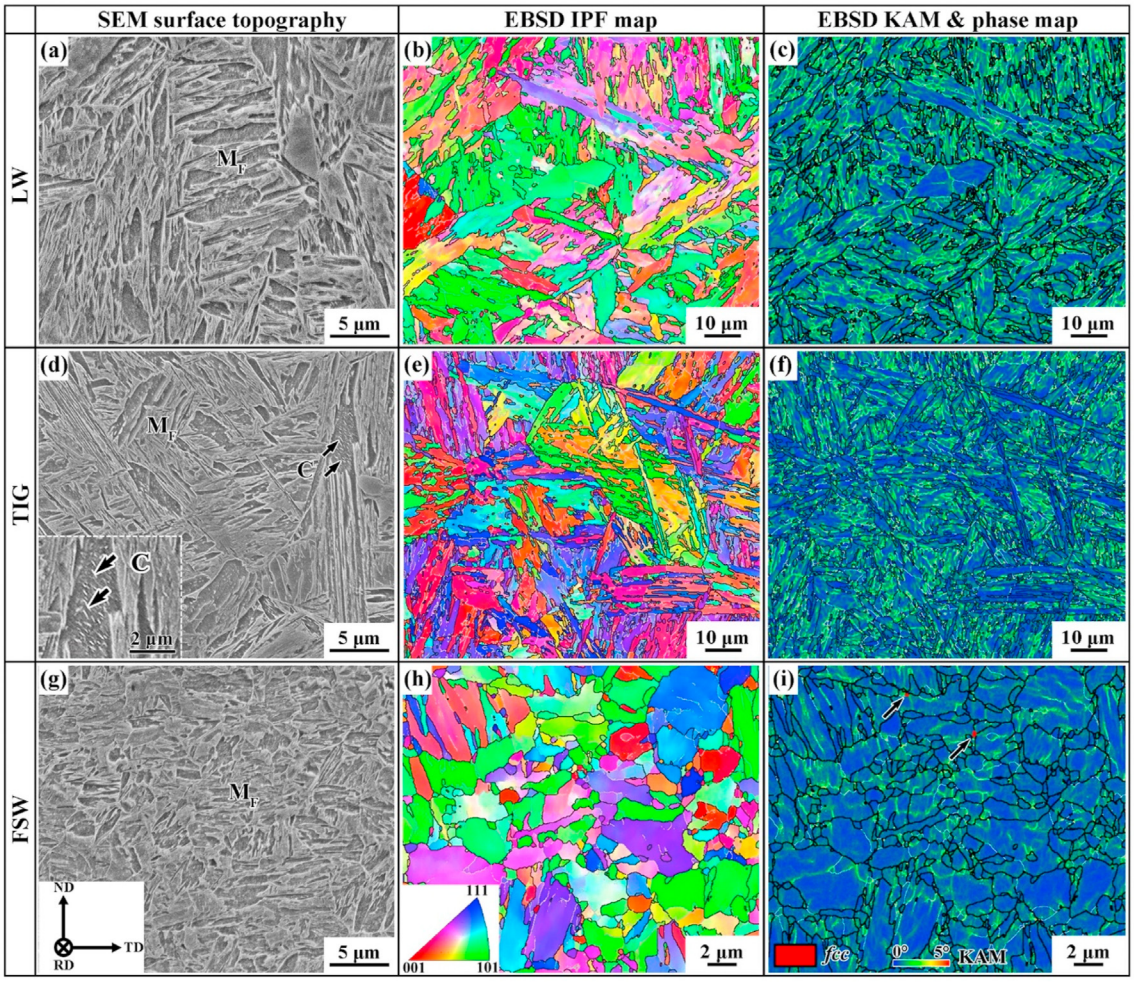

Fig. 4 – SEM and EBSD microstructures of the different WMs.

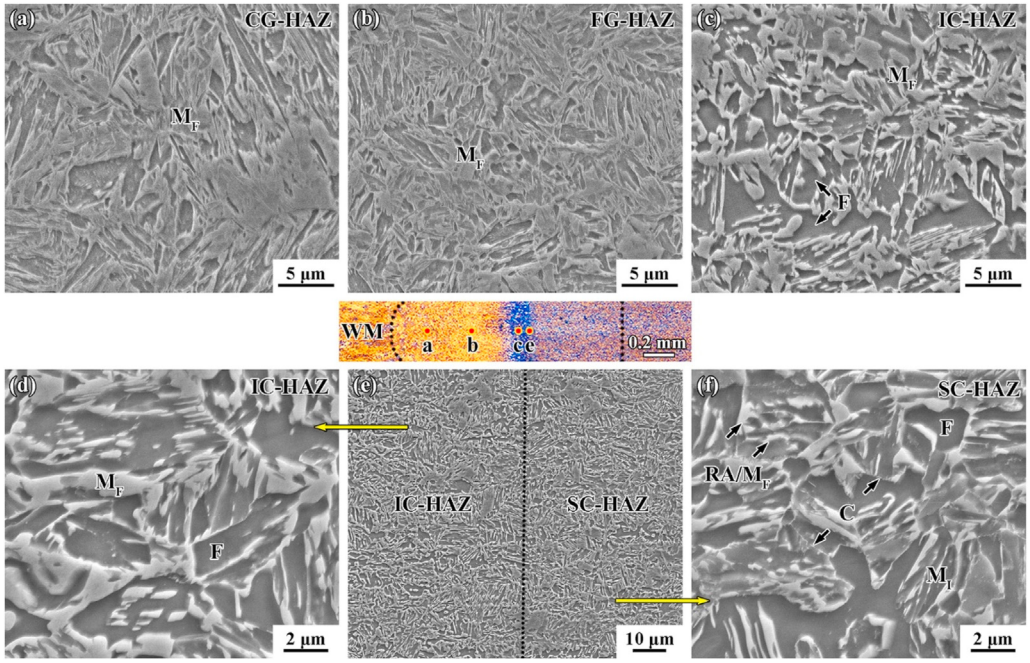

Fig. 5 – SEM micrographs displaying the HAZ microstructure development of the LW joint.

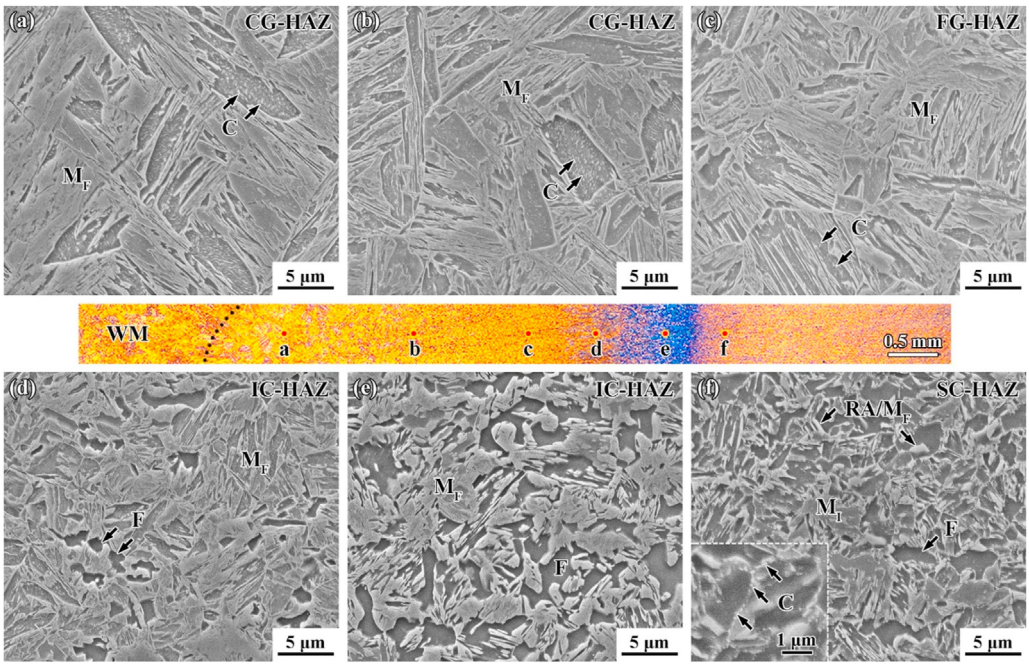

Fig. 6 – SEM micrographs displaying the HAZ microstructure development of the TIG welded joint.

cooling. Thus, no obvious coarsening of the microstructure was observed and similar ultrafine grains were obtained after FSW, compared to the PM (Figs. 3a, d and 4g). Different from the LW and FSW joints, a large number of carbide particles were identified in the laths of martensite for the TIG welded joint (inset in Fig. 4d), which was relevant to the self-

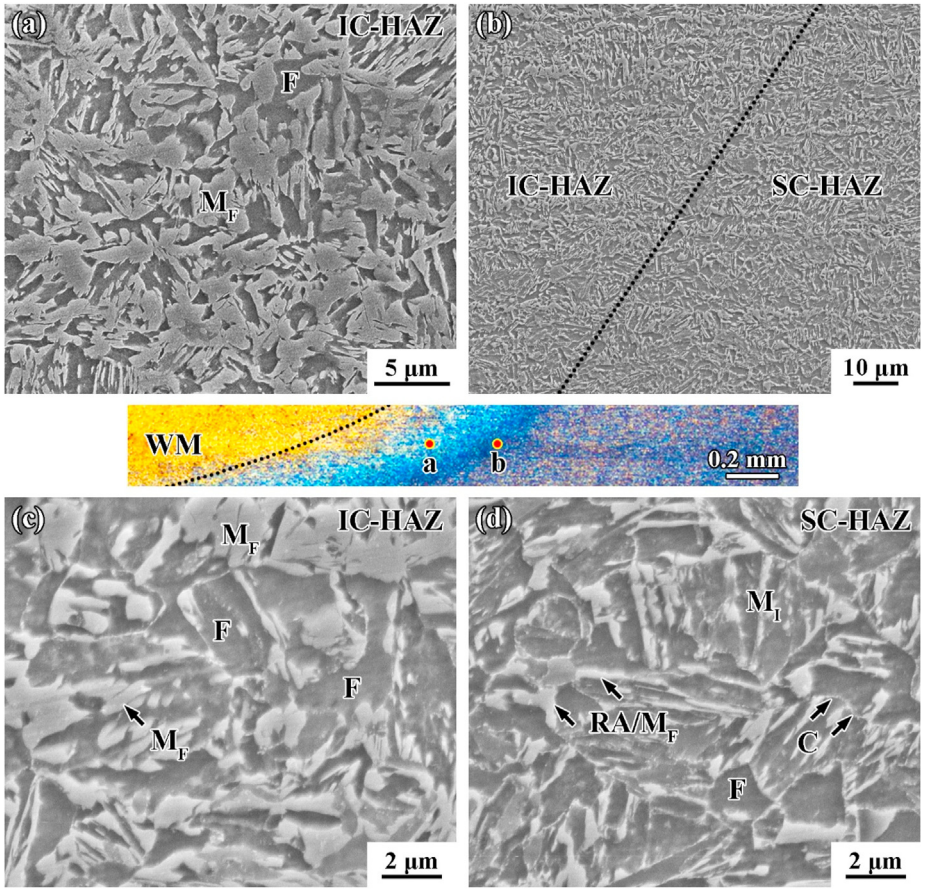

Fig. 7 – SEM micrographs displaying the HAZ microstructure development of the FSW joint.

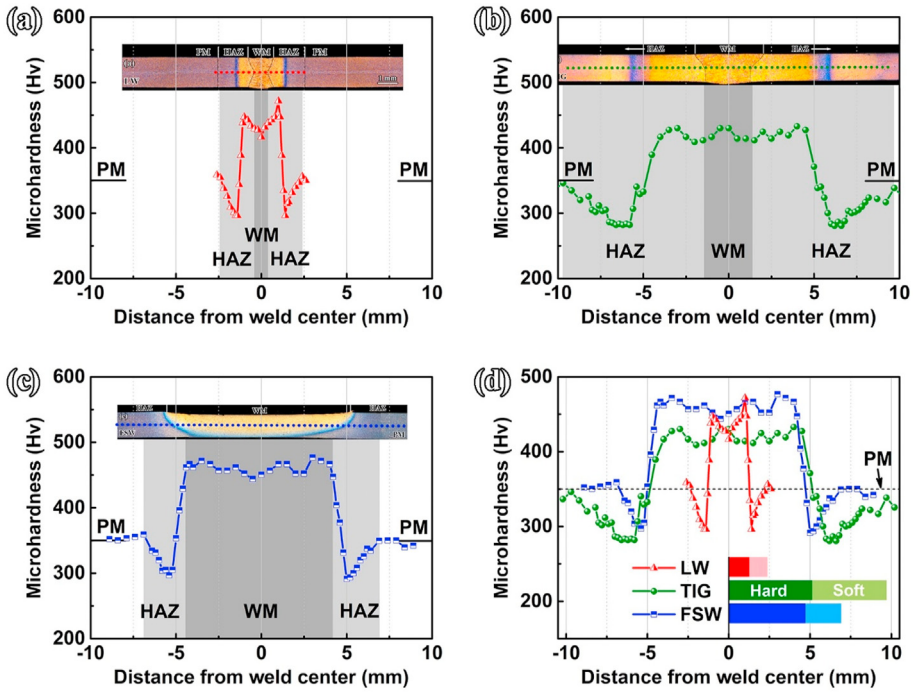

Fig. 8 – Microhardness distribution profiles of the welded joints: (a) LW, (b) TIG welding, (c) FSW, (d) assembly graph.

tempering precipitation during a high-temperature duration with a long time via a high linear energy (Table 2).

The EBSD results of Fig. 4b, e and h exhibited that there was no obvious preferential texture among the martensite packets but approximate orientation which was observed within the packet due to the directional growth of the lath bundle [42]. In the FSW joint, the packet was hardly developed in martensite due to an ultrafine structure size of 0.82 μm. Instead, penetrating lath bundles between adjacent prior austenite boundaries could be observed (Fig. 4h). In addition, the proportions of low angle grain boundaries (misorientation angles between 2 and 15°, gray lines in IPF maps) were 20% and 23% for the WMs of LW and TIG welding respectively, while a lower proportion of 12% was measured for that of the FSW. This was related to the lower density of martensitic substructures such as packets, lath bundles and dislocations, which could be verified by the low kernel average misorientation (KAM) in Fig. 4i. After the thermal or mechanical interaction and phase transformation, the austenite was hard to be retained in the WMs for all welding methods, as displayed in the phase maps of Fig. 4c, f and i.

Under various heating and cooling conditions, the HAZ which was adjacent to the WM without fusion or severe plastic deformation also exhibited significant differences in macroscopic features and microstructures. Fig. 5 shows the HAZ morphologies of the LW joint. The HAZ was comprised of four subregions which were coarse-grained HAZ (CG-HAZ), fine-grained HAZ (FG-HAZ), inter-critical HAZ (IC-HAZ) and sub-critical HAZ (SC-HAZ). As reported in the previous studies [22,25,35,43,44], the peak temperature in the CG-HAZ was similar to that in the WM. The FG-HAZ owned a peak temperature exceeded the A_{c3} temperature but was lower than that in the CG-HAZ. The peak temperature in the IC-HAZ and SC-HAZ was between A_{c3} and A_{c1} (746 °C [27]) and below A_{c1} temperature, respectively. Accordingly, similar fresh martensite was produced in the CG-HAZ (Fig. 5a) compared to that in the WM (Fig. 4a), while a finer martensitic structure was developed in the FG-HAZ (Fig. 5b) via suppressing grain growth at the lower peak temperature in comparison with the CG-HAZ.

In the IC-HAZ, a DP structure of ferrite and martensite was generated. As shown in Fig. 5c, the martensite was convex with high brightness versus the ferrite. Fig. 5d–f reveals the microstructural evolution between IC-HAZ and SC-HAZ, where the interface was marked with a black dotted line (Fig. 5e). It was distinct that ultrafine structures comparable to that in the PM were found in both the IC-HAZ and SC-HAZ. Under the low-temperature aging below A_{c1}, tempering-induced decomposition of martensite and retained austenite occurred in the SC-HAZ, which caused the precipitation of carbide (C) particles (Fig. 5f).

In the TIG welded joint, broad HAZs with comparable microstructure characteristics were observed as contrasted with the LW joint (Fig. 6). Two sites were chosen in the CG-HAZ that a smaller martensitic structure was found at the location far from the WM (Fig. 6b) than that adjacent to the

Table 3 – Geometries and hardness of the three joints.

Welding method	HAZ width (mm)	Hard zone width (mm)	Soft zone width (mm)	Minimum hardness of soft zone (Hv)
LW	2.05	1.28	1.10	296
TIG	8.28	5.14	4.54	281
FSW	2.73	4.72	2.21	295

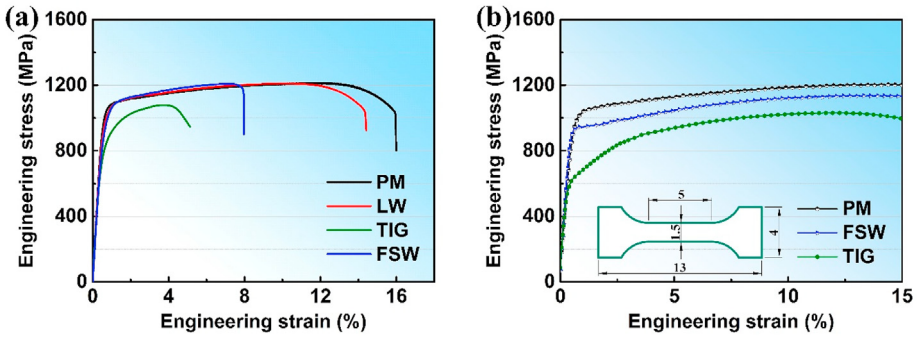

Fig. 9 – Engineering stress-strain curves of the welded joints (a) and the typical soft zones (b).

WM (Fig. 6a). As shown in Fig. 6c, refined martensite was produced in the FG-HAZ. It should be noted that the grain size of prior austenite and the lath width of martensite within the CG-HAZ or FG-HAZ were larger than those observed in the LW joint (Fig. 5a and b). This was attributed to the grain growth induced by a longer duration time at a high temperature during TIG welding, and thus promoted the self-tempering induced precipitation of carbide particles in the CG-HAZ and FG-HAZ, similar to the WM. In the IC-HAZ, the microstructures at adjacent two positions were examined as revealed in Fig. 6d and e. It was obvious that the martensite fraction decreased with the peak temperature declining, which was embodied by the distance increasing away from the WM. In the SC-HAZ of the TIG welded joint, a larger number of carbide particles were found (Fig. 6f) due to more serious tempering precipitation via the larger linear energy and lower cooling rate, compared to the LW joint.

Fig. 7 exhibited the microstructures of HAZ for the FSW joint. Smaller HAZs were generated due to the lower peak temperature and linear energy, compared to the TIG welded joint. The CG-HAZ and FG-HAZ mentioned above were not found in the FSW joint, while only the IC-HAZ and SC-HAZ were visible. Compared with the LW joint, similar microstructures were observed in the IC-HAZ and SC-HAZ with the DP (Fig. 7a and c) and tempered complex structures (Fig. 7d) respectively. Similar to the LW, the precipitation of carbide particles was suppressed by FSW via the low linear energy, under which the carbide particles were hard to be found with a smaller quantity than that observed in TIG welded joint (Fig. 6f).

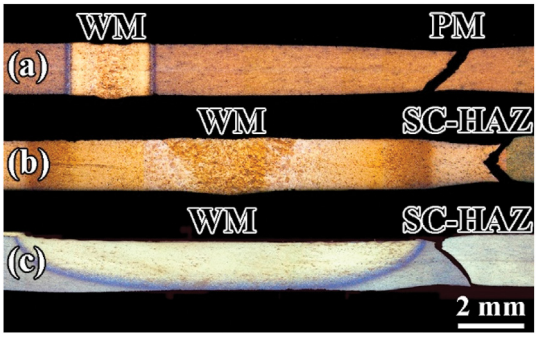

Fig. 10 – Cross-sectional images of (a) LW, (b) TIG welding and (c) FSW joints after tensile tests.

3.3. *Mechanical properties*

Fig. 8 demonstrates the microhardness evolution of the joints. The measured positions were sketched by dotted lines in the inserted OM images. The WM and HAZ of each joint could be discriminated by different background colors according to the OM contrast and hardness evolution (Fig. 8a–c). By contrast with the hardness of the PM, hard zones which possessed higher hardness values and soft zones which owned lower hardness values were differentiated in all of the three welded joints (Fig. 8d). The results indicated that the hardness profile across the joint altered considerably depending on the welding method adopted. The peak hardness of the LW joint was located in the FG-HAZ and the hardness values gradually decreased close to the weld center (Fig. 8a). However, no gradient hardness evolution was found in the hard zones of the TIG welded joint (Fig. 8b) and FSW joint (Fig. 8c). This phenomenon was relevant to the gradual decrease of martensite size from WM to FG-HAZ in the LW joint [43], as shown in Figs. 4a and 5a, b, while the size gradient was inconspicuous in the TIG welded joint (Figs. 4d and 6a–c), causing the negligible hardness gradient in the hard zone. In addition, the FSW joint and TIG welded joint had the highest (450 Hv) and the lowest (417 Hv) average hardness of the hard zones on account of the grain refinement hardening and self-tempering softening, respectively (Fig. 8d).

The widths of HAZ, hard zone, and soft zone were quantified and listed in Table 3 (half of the actual value). Combined with Fig. 8d, a conclusion could be made that the widths of the three joints obeyed the same order of LW < FSW < TIG, which tied in with the sequence of the linear energies (Table 2). The minimal hardness of the soft zone was measured at the boundary between the IC-HAZ and the SC-HAZ for all of the three joints (Figs. 5e and 7b), which was due to the increasing

Table 4 – Mechanical properties of the three welded joints.

Welding method	YS (MPa)	UTS (MPa)	TEL (%)	Failure location
PM	1048 ± 9	1214 ± 5	15 ± 1	–
LW	1028 ± 6	1213 ± 2	13 ± 0.7	PM
TIG	841 ± 5	1082 ± 2	4.4 ± 0.2	Soft zone
FSW	1000 ± 4	1208 ± 2	7 ± 0.5	Soft zone

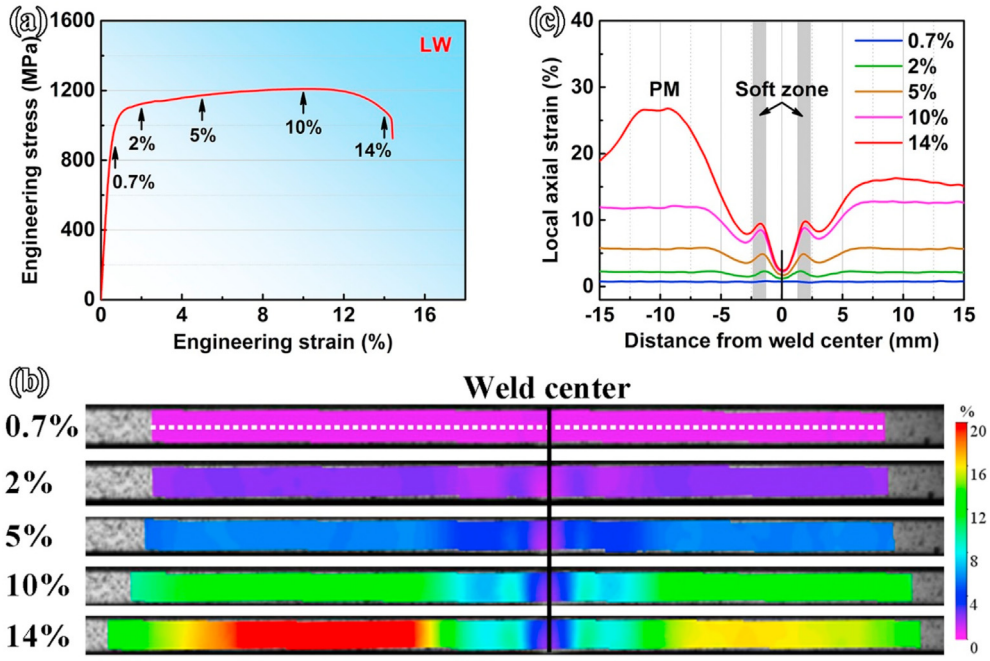

Fig. 11 – Local strain evolution of the LW joint: (a) typical strain stages marked on stress-strain curve, (b) local strain distributions at different tensile strain stages, (c) local strain profiles extracted from (b) along with the cross-sectional center thickness.

of ferrite fraction in the IC-HAZ (compare Fig. 6d with e) and the tempering-induced softening in the SC-HAZ (Figs. 5f, 6f and 7d). Comparable results were reported in the welding of DP steel [44], Q&P steels [25,30], TRIP steel [15] and martensitic steel [43]. The minimum hardness values were shown in Table 3. It revealed that the TIG welded joint owned the lowest hardness (281 Hv) with the most serious material softening (80% of the PM), while the softening degree of the LW and FSW joints was alleviated with enhanced minimum hardness (~295 Hv) due to low linear energy and peak temperature, respectively.

The tensile properties of the Q&P 1180 PM as well as different joints were exhibited in Fig. 9. The YS, UTS and TEL which were obtained based on the engineering stress-strain

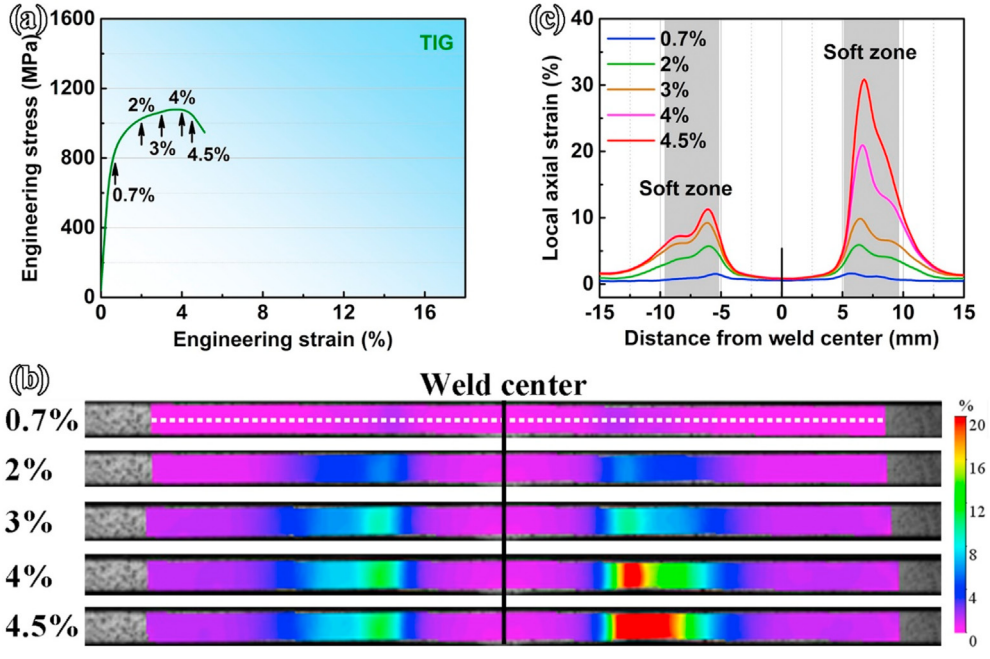

Fig. 12 – Local strain evolution of the TIG welded joint: (a) typical strain stages marked on stress-strain curve, (b) local strain distributions at different tensile strain stages, (c) local strain profiles.

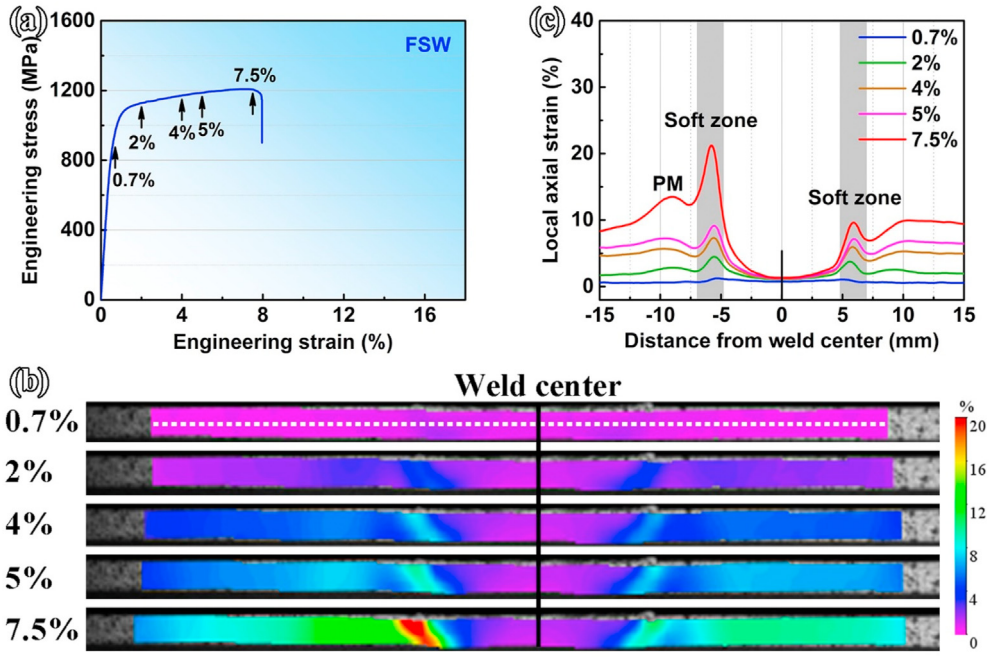

Fig. 13 – Local strain evolution of the FSW joint: (a) typical strain stages marked on stress-strain curve, (b) local strain distributions at different tensile strain stages, (c) local strain profiles.

curves were listed in Table 4. The PM possessed a high strength-ductility synergy. After LW, no distinct variation on the UTS occurred except slight reductions in the YS and TEL. The UTS of the FSW joint was as high as that of the PM, while the YS and TEL decreased by 48 MPa and 8%. For the TIG welded joint, the YS, UTS and TEL were reduced by ~200 MPa, ~130 MPa and ~10% respectively, which were dramatically lower than that of the PM. In the present study, we conclude that the width and minimum hardness of the soft zone play critical roles in the tensile properties of welds. When the soft zone width was too large (4.54 mm for the current study) or the minimum hardness was much less than the average hardness of PM (below 80% of PM for example), strain localization and premature fracture would occur in the soft zone during tensile deformation and thus result in a substantial deterioration of strength and ductility [6,45], such as the joint produced by TIG welding. The diversity of TEL between LW and FSW joints was also attributed to the inhomogeneous strains that evolved across the joint, where heterogeneous microstructures and hardness were produced. More prominent strain localization would occur in the FSW joint due to larger sizes of the hard zone and soft zone, which engendered larger ductility loss of the FSW joint.

In this research, no evident variation was detected in the YS and UTS of LW and FSW joints even though a hardness reduction of ~55 Hv was formed, compared to the PM. That is, the strength, especially the UTS of the joint was impervious to the softened HAZ. To clarify this issue, non-standard mini tensile specimens with a gauge dimension of $5 \times 1.5 \times 0.6$ mm^3 (inset in Fig. 9b) were incised from the soft zone along the RD. Note that the PM and the soft zone of the TIG welded joint were also tested under the same circumstance for comparison, while the assessment of the LW joint was not carried out due to the limited soft zone width. As shown in Fig. 9b, it was apparent that the soft zone of the TIG weld yielded earlier than that of the FSW joint and PM as the result of severe tempering softening. By suppressing the material softening via reducing the welding linear energy, the YS of the soft zone was effectively enhanced by using FSW, although the equal YS to the PM was hard to be achieved. Recently, some reports suggested that the special macrostructural configuration such as in LW [46] and FSW [30] joints could provide additional macrostructure strengthening in achieving joints without strength loss. Under tensile strain, the PM remained in a uniaxial stress state, while a biaxial stress state could appear in the soft zone with an extra stress which could offset a portion of applied stress, and thereby counteract the strength loss caused by the material softening.

3.4. *Failure mechanism*

As shown in Table 4, the failure behavior of the welded joint was influenced by the welding method used. The TIG welded and FSW joints fractured in the soft zone whereas the LW joint was broken in the PM. As displayed in Fig. 10, the LW joint was broken at the location far away from the weld center. However, the fracture was clearly observed in the SC-HAZ for the other two joints. In general, the fracture location was strongly related to the joint's material softening which caused strain concentration and eventual necking failures [15], such as the current joints of TIG welding and FSW. Nevertheless, this inference was not working anymore in the LW joint. To understand this phenomenon, the in-situ strain evolution on the cross-sectional surface was investigated via the DIC technique.

As depicted in Fig. 11a, several total tensile strains were selected as the typical strain stages for the LW joint. The obtained local axial strain profiles which were extracted from the extensional strain distributions of Fig. 11b were shown in Fig. 11c. It was clear that no distinct strain concentration was found across the joint near the yielding stage (0.7% total strain), while the strain concentration first occurred in the soft zone at the work hardening stage (2% total strain) with local strain as high as that in the PM. With the tensile load increasing, the PM gradually seized the initiative in plastic strain (5% total strain) and enlarged its advantage at the peak load stage (10% total strain). Ultimately, necking was developed in the PM with a large local strain concentration (14% total strain). As described above, it was noteworthy that there existed a competitive relationship between the soft zone and PM, that the soft zone turned the tide of strain hardening during plastic deformation and resulted in the failure in the PM.

As for the TIG welded joint, the strain trade-off between soft zone and PM was not found anymore. As shown in Fig. 12, strain concentration in the soft zone was observed during the whole tensile deformation. At the peak load stage (4% total strain), an ultrahigh local strain of more than 20% was measured in the soft zone. This was much greater than that found in the LW joint (10% total strain in Fig. 11c) and verified the above discussions on the strain localization and premature fracture. Nevertheless, the one-sided strain concentration in the soft zone could be restrained by FSW, while obvious strain partitioning from soft zone to PM occurred in Fig. 13b and c. This reappearance of local strain interaction indicated an enhanced strain hardening ability of the soft zone. Together with the macrostructure strengthening, the premature strain localization and fracture were effectively delayed and thus high strength joints with considerable elongations were achieved after FSW, which is comparable with the LW. In addition, it was suggested that the diversity of the fracture locations between LW and FSW joints was relevant to the soft zone width. A narrow soft zone would provide a small strain concentration region, heighten the extra stress in the biaxial stress state, and consequently avoid necking in the soft zone [30].

4. Conclusions

The weldability of an ultrahigh-strength Q&P 1180 steel was systematically studied by comparing the microstructures and mechanical properties of variant welded joints fabricated by LW, TIG welding, and FSW. The main conclusions can be drawn as follows:

1. Defect-free welded joints which consisted of WM, HAZ and PM were successfully produced although obvious differences in the size and morphology of these regions were observed. The width of the WM and HAZ were strongly related to the linear energy of a certain welding method (LW < FSW < TIG welding). Exceptionally, FSW owned the maximal WM width due to the largest heat source area which was determined by the tool dimension.
2. After LW and TIG welding, the PM was totally destroyed in the WMs, and coarse lath martensite was generated due to materials remelting and high-temperature duration. However, refined martensite with ultrafine grains which were comparable to that in the PM was obtained after FSW because of the low peak temperature and severe plastic deformation effect.
3. Four subregions of CG-HAZ, FG-HAZ, IC-HAZ and SC-HAZ were distinguished in the HAZ. However, the CG-HAZ and FG-HAZ were not found in FSW joint. In CG-HAZ and FG-HAZ, fresh martensite was produced with a gradual decrease of the structural sizes from the former to the latter. The IC-HAZ was comprised of a DP structure, while carbide precipitation usually occurred in the SC-HAZ owing to the tempering-induced decomposition of martensite and retained austenite.
4. Apparent hard zones and soft zones were differentiated in all of the three welded joints based on the hardness profiles which altered considerably depending on the welding method adopted. The TIG welding produced the most serious material softening (20% reduction relative to the PM), while the softening degree was alleviated via LW and FSW due to the low linear energy and peak temperature, respectively.
5. Excellent tensile strength as high as that of the PM was achieved in both the LW and FSW joints. However, dramatical losses of the YS, UTS and TEL were found in the TIG welded joint, which was attributed to the premature strain localization and fracture in the soft zone. By using LW and FSW, the strain localization was effectively delayed and thus high strength joints with considerable ductility were achieved.

Declaration of Competing Interest

The authors declare that they have no known competing financial interests or personal relationships that could have appeared to influence the work reported in this paper.

Acknowledgments

This work was supported by the National Natural Science Foundation of China under Grant Nos. 51901225, 51671190, 52171057 and 52034005, Liaoning Province Excellent Youth Foundation (2021-YQ-01), and the Open Research Fund from the State Key Laboratory of Rolling and Automation, Northeastern University (2020RALKFKT009).

REFERENCES

[1] Matlock DK, Bräutigam VE, Speer JG. Application of the quenching and partitioning (Q&P) process to a medium-carbon, high-Si microalloyed bar steel. Mater Sci Forum 2003;426–423:1089–94. https://doi.org/10.4028/www.scientific.net/MSF.426-432.1089.

[2] Edmonds DV, He K, Rizzo FC, De Cooman BC, Matlock DK, Speer JG. Quenching and partitioning martensite—a novel steel heat treatment. Mater Sci Eng, A 2006;438–440:25–34. https://doi.org/10.1016/j.msea.2006.02.133.

[3] Speer JG, Rizzo Assunção FC, Matlock DK, Edmonds DV. The "quenching and partitioning" process: background and recent progress. Mater Res 2005;8:417–23. https://doi.org/10.1590/S1516-14392005000400010.
[4] Zhao JW, Jiang ZY. Thermomechanical processing of advanced high strength steels. Prog Mater Sci 2018;94:174–242. https://doi.org/10.1016/j.pmatsci.2018.01.006.
[5] Dai ZB, Chen H, Ding R, Lu Q, Zhang C, Yang ZG, et al. Fundamentals and application of solid-state phase transformations for advanced high strength steels containing metastable retained austenite. Mater Sci Eng R 2021;143:100590. https://doi.org/10.1016/j.mser.2020.100590.
[6] Lee JH, Park SH, Kwon HS, Kim GS, Lee CS. Laser, tungsten inert gas, and metal active gas welding of DP780 steel: Comparison of hardness, tensile properties and fatigue resistance. Mater Des 2014;64:559–65. https://doi.org/10.1016/j.matdes.2014.07.065.
[7] Sharma RS, Molian P. Yb:YAG laser welding of TRIP780 steel with dual phase and mild steels for use in tailor welded blanks. Mater Des 2009;30:4146–55. https://doi.org/10.1016/j.matdes.2009.04.033.
[8] Lu L, Liang ZX, Yang J, Sun Q, Zhu TC, Wang XN. Investigation on laser welding of a novel hot-stamped steel with 2000 MPa. J Mater Res Technol 2020;9:13147–52. https://doi.org/10.1016/j.jmrt.2020.09.044.
[9] Hernandez VHB, Kuntz ML, Khan MI, Zhou Y. Influence of microstructure and weld size on the mechanical behaviour of dissimilar AHSS resistance spot welds. Sci Technol Weld Join 2008;13:769–76. https://doi.org/10.1179/136217108X325470.
[10] Pouranvari M, Marashi SPH, Safanama DS. Failure mode transition in AHSS resistance spot welds. Part II: Experimental investigation and model validation. Mater Sci Eng, A 2011;528:8344–52. https://doi.org/10.1016/j.msea.2011.08.016.
[11] Siar O, Dancette S, Dupuy T, Fabrègue D. Impact of liquid metal embrittlement inner cracks on the mechanical behavior of 3 generation advanced high strength steel spot welds. J Mater Res Technol 2021. https://doi.org/10.1016/j.jmrt.2021.11.100.
[12] Ahiale GK, Oh YJ. Microstructure and fatigue performance of butt-welded joints in advanced high-strength steels. Mater Sci Eng A 2014;597:342–8. https://doi.org/10.1016/j.msea.2014.01.007.
[13] Ohashi R, Fujimoto M, Mironov S, Sato YS, Kokawa H. Effect of contamination on microstructure in friction stir spot welded DP590 steel. Sci Technol Weld Join 2009;14:221–7. https://doi.org/10.1179/136217108x388642.
[14] Wang ZW, Ma GN, Yu BH, Xue P, Xie GM, Zhang H, et al. Improving mechanical properties of friction-stir-spot-welded advanced ultra-high-strength steel with additional water cooling. Sci Technol Weld Join 2020;25:336–44. https://doi.org/10.1080/13621718.2019.1706259.
[15] Mironov S, Sato YS, Yoneyama S, Kokawa H, Fujii HT, Hirano S. Microstructure and tensile behavior of friction-stir welded TRIP steel. Mater Sci Eng, A 2018;717:26–33. https://doi.org/10.1016/j.msea.2018.01.053.
[16] Matsushita M, Kitani Y, Ikeda R, Ono M, Fujii H, Chung YD. Development of friction stir welding of high strength steel sheet. Sci Technol Weld Join 2011;16:181–7. https://doi.org/10.1179/1362171810Y.0000000026.
[17] Weber G, Thommes H, Gaul H, Hahn O, Rethmeier M. Resistance spot welding and weld bonding of advanced high strength steels. Mat-wiss u Werkstofftech 2010;41:931–9. https://doi.org/10.1002/mawe.201000687.
[18] Eyvazian A, Hamouda A, Tarlochan F, Derazkola HA, Khodabakhshi F. Simulation and experimental study of underwater dissimilar friction-stir welding between aluminium and steel. J Mater Res Technol 2020;9:3767–81. https://doi.org/10.1016/j.jmrt.2020.02.003.
[19] Clarke AJ, Speer JG, Miller MK, Hackenberg RE, Edmonds DV, Matlock DK, et al. Carbon partitioning to austenite from martensite or bainite during the quench and partition (Q&P) process: a critical assessment. Acta Mater 2008;56:16–22. https://doi.org/10.1016/j.actamat.2007.08.051.
[20] Toji Y, Matsuda H, Herbig M, Choi P-P, Raabe D. Atomic-scale analysis of carbon partitioning between martensite and austenite by atom probe tomography and correlative transmission electron microscopy. Acta Mater 2014;65:215–28. https://doi.org/10.1016/j.actamat.2013.10.064.
[21] Derazkola HA, Gil EG, Murillo-Marrodán A, Méresse D. Review on dynamic recrystallization of martensitic stainless steels during hot deformation: part I—Experimental study. Metals 2021;11:572. https://doi.org/10.3390/met11040572.
[22] Guo W, Wan ZD, Peng P, Jia Q, Zou GS, Peng Y. Microstructure and mechanical properties of fiber laser welded QP980 steel. J Mater Process Technol 2018;256:229–38. https://doi.org/10.1016/j.jmatprotec.2018.02.015.
[23] Li WD, Ma LX, Peng P, Jia Q, Wan ZD, Zhu Y, et al. Microstructural evolution and deformation behavior of fiber laser welded QP980 steel joint. Mater Sci Eng A 2018;717:124–33. https://doi.org/10.1016/j.msea.2018.01.050.
[24] Xue JL, Peng P, Guo W, Xia MS, Tan CW, Wan ZD, et al. HAZ characterization and mechanical properties of QP980-DP980 laser welded joints. Chin J Mech Eng 2021;34:1–14. https://doi.org/10.1186/s10033-021-00596-x.
[25] Lin HT, Jiang HT, Wang YS, Tian SW. Microstructure gradient characteristics and mechanical properties of friction stir welded high strength QP980 steel. Mater Res Express 2019;6:126584. https://doi.org/10.1088/2053-1591/ab5a92.
[26] Wu XY, Lin HT, Luo W, Jiang HT. Microstructure and microhardness evolution of thermal simulated HAZ of Q&P980 steel. J Mater Res Technol 2021;15:6067–78. https://doi.org/10.1016/j.jmrt.2021.11.059.
[27] Wang ZW, Zhang H, An XH, Wu LH, Xue P, Zhang QC, et al. Achieving equal strength joint to parent metal in a friction stir welded ultra-high strength quenching and partitioning steel. Mater Sci Eng, A 2020;793:139979. https://doi.org/10.1016/j.msea.2020.139979.
[28] Memon S, Tomków J, Derazkola HA. Thermo-mechanical simulation of underwater friction stir welding of low carbon steel. Materials 2021;14:4953. https://doi.org/10.3390/ma14174953.
[29] Derazkola HA, García E, Eyvazian A, Aberoumand M. Effects of rapid cooling on properties of aluminum-steel friction stir welded joint. Materials 2021;14:908. https://doi.org/10.3390/ma14040908.
[30] Wang ZW, Zhang JF, Xie GM, Wu LH, Zhang H, Xue P, et al. Evolution mechanisms of microstructure and mechanical properties in a friction stir welded ultrahigh-strength quenching and partitioning steel. J Mater Sci Technol 2022;102:213–23. https://doi.org/10.1016/j.jmst.2021.06.031.
[31] Marconi CD, Svoboda HG. Welding of advanced high strength steels for automotive applications. In: da Silva FJG, de Bastos Pereira AM, editors. Handbook of welding: processes, control and simulation. New York: Nova Science Publishers; 2021. p. 1–44.
[32] Mishra RS, Ma ZY. Friction stir welding and processing. Mater Sci Eng R 2005;50:1–78. https://doi.org/10.1016/j.mser.2005.07.001.
[33] Zhang H, Wang D, Xue P, Wu LH, Ni DR, Xiao BL, et al. Achieving ultra-high strength friction stir welded joints of high nitrogen stainless steel by forced water cooling. J Mater Sci Technol 2018;34:2183–8. https://doi.org/10.1016/j.jmst.2018.03.014.

[34] Tehrani-Moghadam HG, Jafarian HR, Heidarzadeh A, Eivani AR, Do H, Park N. Superior mechanical properties in high-Ni transformation induced plasticity steels after friction stir welding. J Mater Res Technol 2020;9:5431–41. https://doi.org/10.1016/j.jmrt.2020.03.069.
[35] Di HS, Sun Q, Wang XN, Li JP. Microstructure and properties in dissimilar/similar weld joints between DP780 and DP980 steels processed by fiber laser welding. J Mater Sci Technol 2017;33:1561–71. https://doi.org/10.1016/j.jmst.2017.09.001.
[36] Frigaard Ø, Grong Ø, Midling OT. A process model for friction stir welding of age hardening aluminum alloys. Metall Mater Trans 2001;32:1189–200. https://doi.org/10.1007/s11661-001-0128-4.
[37] Das Lala S, Biswas A, Debbarma J, Deoghare AB. Study of hardness of the weld bead formed by partial hybrid welding by metal inert gas welding and submerged arc welding at three different heat inputs. Mater Today Proc 2018;5:13650–7. https://doi.org/10.1016/j.matpr.2018.04.003.
[38] Nandan R, Roy GG, Lienert TJ, Debroy T. Three-dimensional heat and material flow during friction stir welding of mild steel. Acta Mater 2007;55:883–95. https://doi.org/10.1016/j.actamat.2006.09.009.
[39] Imam M, Ueji R, Fujii H. Microstructural control and mechanical properties in friction stir welding of medium carbon low alloy S45C steel. Mater Sci Eng, A 2015;636:24–34. https://doi.org/10.1016/j.msea.2015.03.089.
[40] ASTM standard E1245-03, standard practice for determining the inclusion or second phase constituent content of metals by automatic image analysis. West Conshohocken, PA: ASTM International; 2016.
[41] ASTM standard E8/E8M-13a, standard test methods for tension testing of metallic materials. West Conshohocken, PA: ASTM International; 2013.
[42] Kitahara H, Ueji R, Tsuji N, Minamino Y. Crystallographic features of lath martensite in low-carbon steel. Acta Mater 2006;54:1279–88. https://doi.org/10.1016/j.actamat.2005.11.001.
[43] Luo C, Cao Y, Zhao Y, Zhao L, Shan J. Fiber laser welding of 1700-MPa, ultrahigh-strength steel. Weld J 2018;97:214–28. https://doi.org/10.29391/2018.97.019.
[44] Wang ZW, Xie GM, Wang D, Zhang H, Ni DR, Xue P, et al. Microstructural evolution and mechanical behavior of friction-stir-welded DP1180 advanced ultrahigh strength steel. Acta Metall Sin (Engl Lett) 2020;33:58–66. https://doi.org/10.1007/s40195-019-00949-5.
[45] Derazkola HA, Eyvazian A, Simchi A. Submerged friction stir welding of dissimilar joints between an al-mg alloy and low carbon steel: Thermo-mechanical modeling, microstructural features, and mechanical properties. J Manuf Process 2020;50:68–79. https://doi.org/10.1016/j.jmapro.2019.12.035.
[46] Jia Q, Guo W, Li WD, Peng P, Zhu Y, Zou GS, et al. Experimental and numerical study on local mechanical properties and failure analysis of laser welded DP980 steels. Mater Sci Eng A 2017;680:378–87. https://doi.org/10.1016/j.msea.2016.10.121.